Biomass-Derived Phosphorus-Doped Porous Hard Carbon Anode for Stable and High-Rate Sodium Ion Batteries

Puwu Liang,[a, b] Zijing Huo,[a, b] Yangjie Liu,[b] Zheng Bo,[c] Yongmin Wu,[d] Xiang Hu,*[b] and Zhenhai Wen*[b]

Biomass-derived hard carbon, despite being promising for anode material of sodium-ion batteries, usually suffer from low initial coulombic efficiency (ICE), poor rate capacity, and limited cycling stability caused by complex surface defects and low intrinsic conductivity. Herein, phosphorus-doped porous hard carbon (HC@PC−P) were synthesized by the thermal polymerization of soy lecithin on the surfaces of hard carbon derived from olive kernels. The incorporation of heteroatom phosphorus in the porous hard carbon framework expands the carbon lattice spacing, optimizes the graphitization degree, and increases electrical conductivity, guaranteeing ensuring rapid electron and ion transfer. These coupling effects enable HC@PC−P anode to achieve a high reversible capacity of 350 mAh g^{-1} at 0.1 A g^{-1}, an impressive initial coulombic efficiency of 89.6 %, and remarkable long-term cycling stability at 1 A g^{-1} over 1000 cycles with negligible capacity fade. The mechanisms behind sodium storage and enhanced electrochemical performance were elucidated by ex-situ Raman spectroscopy and kinetic analysis. Additionally, the assembled HC@PC−P//Na$_3$V$_2$(PO$_4$)$_3$ full cell demonstrated a high energy density of 257.9 Wh kg^{-1}. This work provides a rational guide for designing advanced hard carbon anode materials for high-energy sodium-ion batteries.

Introduction

The increasing demand for energy and a heightened focus on sustainable development have led to a significant rise in the use of lithium-ion batteries (LIBs) in electric vehicles, portable electronic devices, and other applications. This surge has intensified the demand for lithium resources, resulting in a gradual tightening of their supply.[1–2] In this context, sodium-ion batteries (SIBs), which operate on principles similar to those of LIBs, emerge as promising candidates for large-scale energy storage applications due to the abundance, wide distribution, and low cost of sodium resources.[3–4] The anode material plays a crucial role in the performance of SIBs. Ideal anode materials should exhibit high specific capacity, good cycling stability, excellent rate performance, and low cost.[5–6] However, sodium ions are larger than lithium ions, which presents greater challenges during the insertion and extraction processes in charge-discharge cycles. This size difference imposes higher challenges to the structure and performance of anode materials for sodium storage.[7]

Biomass materials such as coconut shells,[8] fruit shells,[9] grapefruit peels,[10–11] starches,[12] walnut shells,[13] corn cobs,[14] and various animal and plant tissues[15–16] can serve as precursors for producing hard carbon materials. These raw materials are abundant in nature, with many being byproducts of industrial and agricultural processes, ensuring a plentiful and sustainable source for hard carbon.[17] Moreover, the hard carbon materials derived from biomass possess a complex microstructure, characterized by the stacking of curved graphite-like sheets that form short-range ordered microregions, alongside numerous nanopores.[18–22] This intricate structure offers ample space for sodium ion storage, resulting in a high specific capacity. Despite these advantages, hard carbon materials derived from biomass face significant challenges, including low initial coulombic efficiency (ICE) and poor ion diffusion kinetic, which greatly affect their practical capacity. These issues become especially pronounced during high current charging and discharging, where the embedding and extraction speeds of sodium ions are limited, resulting in poor rate performance.[23]

[a] P. Liang, Z. Huo
     College of Chemistry
     Fuzhou University
     Fuzhou 350002, China

[b] P. Liang, Z. Huo, Y. Liu, X. Hu, Z. Wen
     State Key Laboratory of Structural Chemistry, and Fujian Provincial Key
     Laboratory of Materials and Techniques toward Hydrogen Energy
     Fujian Institute of Research on the Structure of Matter, Chinese Academy of
     Sciences
     Fuzhou, Fujian, 350002, China
     E-mail: huxiang@fjirsm.ac.cn
            wen@fjirsm.ac.cn

[c] Z. Bo
     State Key Laboratory of Clean Energy Utilization, Zhejiang University

[d] Y. Wu
     State Key Laboratory of Space Power-sources Technology, Shanghai
     Institute of Space Power Sources, 2965 Dongchuan Road, Shanghai 200245,
     China

     Supporting information for this article is available on the WWW under
     https://doi.org/10.1002/batt.202400694

Batteries & Supercaps

Research Article
doi.org/10.1002/batt.202400694

Chemistry
Europe

European Chemical
Societies Publishing

In recent years, researchers have made significant strides in optimizing the performance of hard carbon anodes through various modification techniques, such as adjusting the synthesis and carbonization processes of precursors, coating and compounding with other materials, heteroatom doping, electrolyte regulation, and presodiation.[24–26] Sodium ions are stored in hard carbon via mechanisms such as defect adsorption, interlayer insertion, and nanopore filling. Consequently, the sodium storage capacity of hard carbon is heavily influenced by its microstructure. A recent study by Liu et al. introduced a novel instantaneous sintering technology.[27] introduced a novel instantaneous sintering technology that enables precise control over the temperature and duration of thermal pulses. This innovation allows for effective phase regulation of hard carbon anode materials and optimization of nanopore growth. As a result, this method achieves a significantly extended working voltage on the low voltage platform (below 0.1 V) and a discharge capacity of 325 mAh g^{-1}. Given the larger ionic radius of Na$^+$, its kinetic processes are relatively slow, making the design of morphologies that enhance diffusion channels a crucial strategy for improving rate performance. In a complementary approach, Tang et al. utilized biological spores (SCG) as precursors to synthesize hard carbon materials with diverse macro- and microstructures through a coupling strategy.[28] Their resulting material achieved a high-rate performance of 254.88 mAh g^{-1} and cycle stability. Moreover, the construction of Al$_2$O$_3$ and AlF$_3$ coatings on the surface of hard carbon anodes can inhibit the continuous decomposition of the electrolyte and promote the formation of a stable SEI layer.[29–30] Heteroatom doping has emerged as a well-established method for controlling defects and interlayer spacing in hard carbon materials. By introducing heteroatoms (such as N, O, P, S, etc.) and cations (such as Li$^+$, Na$^+$, K$^+$, Ca^{2+}, etc.), researchers can optimize microscopic properties, including interlayer spacing, surface wettability, and electronic conductivity, thereby enhancing sodium storage performance.[31–34] However, it is important to note that the study of heteroatom doping should prioritize elucidating the underlying mechanisms rather than merely focusing on performance indicators. Furthermore, accurately controlling the morphology and compositional structure of hard carbon, as well as achieving fast and stable sodium ion storage, remains a significant challenge.
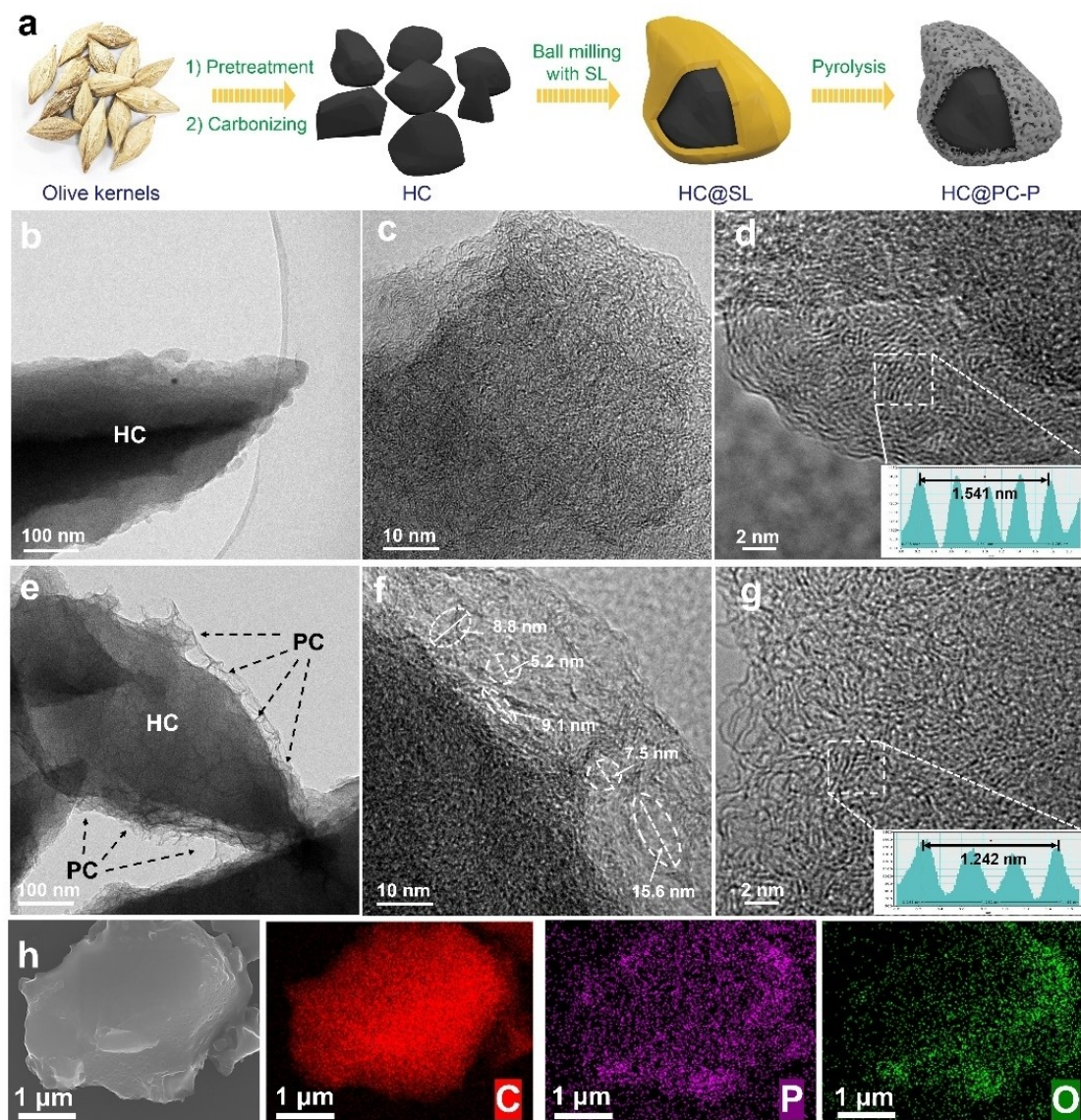
Herein, we present a strategy that simultaneously regulates pore design and heteroatom (P) doping by integrating natural soy lecithin with the surface of hard carbon derived from the carbonization of waste biomass precursors (olive kernel). Compared with pure hard carbon materials, the modified phosphorus-doped porous hard carbon (HC@PC–P) material features abundant mesoporous structures on its surface and incorporates heteroatoms. The resulting HC@PC–P demonstrates a high reversible specific capacity of 350 mAh g^{-1} at 0.1 A g^{-1} and ICE of 89.6%, surpassing most previously reported biomass-derived carbons for SIB applications. Additionally, it exhibits excellent long-term cycle stability, with a capacity retention rate of 93.9% after 1000 cycles at 1 A g^{-1} and fast sodium storage kinetics. When combined with a Na$_3$V$_2$(PO$_4$)$_3$ cathode, the full battery exhibits a high energy density and robust cycle life. Our research not only confirms the synergistic effects of pore structure and heteroatom doping in enhancing sodium storage capacity but also demonstrates the potential of transforming waste products into advanced biomass-based hard carbon materials, offering significant promise for developing high-performance, low-cost commercial anode materials for SIBs.

Results and Discussion

The scanning electron microscopy (SEM) and transmission electron microscopy (TEM) images shown in Figures 1 and S1–3 clearly present the morphological and micro structural changes of olive kernel derived hard carbon before and after modification with soy lecithin following high-temperature pyrolysis. From the SEM images (Figures S1a and S1b), it can be observed that the pure olive kernel derived hard carbon presents an irregular block like morphology, characterized by a limited number of small nanoparticles attached to the outer surfaces of larger particles measuring several microns. In Figures S2a and S2b, the carbonized pure soy lecithin displays a porous structure. Figure S3a reveals that the modified hard carbon retains an irregular block-like structure at low magnification, while high-magnification analysis in Figure S2b shows a uniform and dense texture on the outer surface, featuring noticeable pores. Elemental mapping (Figure 1h) shows that C, O, and P are evenly distributed in HC@PC–P, confirming the success of our P doping strategy. The TEM image (Figure 1e) further supports the observation that the dense structure on the surface of HC@PC–P consists of pores formed during the carbonization of soy lecithin, as shown in Figure 1f, which reveals that these pores are mesoporous, ranging from several nanometers to dozens of nanometers. This porous architecture facilitates electrolyte penetration and provides ample channels for the rapid diffusion of sodium ions. Further investigation of the detailed lattice structure of HC@PC–P was conducted using high resolution transmission electron microscopy (HRTEM) analysis (Figure 1g). The results indicate the presence of typical amorphous carbon with short-range graphite domains, characterized by a broken and distorted carbon lattice. The estimated lattice fringe measures 0.41 nm, which exceeds the interlayer spacing of pure hard carbon (0.38 nm) as depicted in Figure 1d. This increase in interlayer spacing is likely attributed to the incorporation of phosphorus doping.

The samples were characterized by X-ray diffraction (XRD) (Figure 2a). The XRD pattern shows two broad diffraction peaks centered at $2\theta = 23.5°$ and $43.6°$, which belong to the (002) and (101) crystal planes of graphite carbon, respectively.[35] Notably, compared to HC, the (002) peak of HC@PC–P exhibits a smaller shift, with a value of 21.5°. According to the Bragg equation, the interlayer distance of HC@PC–P is 0.411 nm, while that of HC is 0.377 nm. This finding aligns with the HRTEM imaging results, which reveal the thickness and average length of the obtained graphite-like nanocrystalline domains, designated as Lc and La (Table S1).[36] Figure 2b presents the Raman spectra of the materials, revealing two characteristic peaks at 1343 cm^{-1}

Batteries & Supercaps

Research Article
doi.org/10.1002/batt.202400694

Chemistry Europe
European Chemical
Societies Publishing

Figure 1. a) Schematic illustration of the synthetic process for HC@PC–P. Morphologies of prepared HC@PC–P and HC. b–c) TEM images, and d) HR-TEM image of HC (inset: lattice fringes of HC and its corresponding interlayer distances). E–f) TEM images, and g) HR-TEM image of HC@PC–P (inset: lattice fringes of HC@PC–P and its corresponding interlayer distances). h) SEM image of HC@PC–P and the corresponding EDS element mapping of C, P and O.

and 1594 cm^{-1}, which correspond to the degree of disorder and graphitization, respectively.[37] Notably, PC exhibits the highest degree of graphitization, while HC has the most defects. The HC@PC–P displays an I_D/I_G value of 1.03, falling between the values of PC (0.97) and HC (1.10). The reduction in defects is beneficial for minimizing the irreversible loss of Na$^+$ and for forming a structurally stable SEI layer.

To comprehensively characterize the closed pores in the hard carbon samples, small-angle X-ray scattering (SAXS) tests were conducted. The SAXS curve reveals a broad hump in the scattering vector Q from 1 to 2 nm^{-1}.[38–39] These humps are indicative of closed pores in the carbon matrix, encompassing both micron-sized and nanometer-sized voids between sp2 graphite layers.[40–42] As observed in the SAXS curve (Figure 2c), HC@PC–P and HC display more pronounced wide humps at

approximately 0.1 Å^{-1} compared to PC, suggesting an increase in closed pore radius and a higher abundance of closed pores. The SAXS data were analyzed using a previously developed hard carbon model. As shown in Table S1, the fitted closed micropore diameter of HC@PC–P is 1.706 nm, slightly lower than 2.315 nm of HC. This reduction is attributed to the PC layer coating the surface of HC, which marginally decreases the closed pore radius of HC@PC–P.

The specific surface area and pore size distribution of the materials were analyzed through N$_2$ adsorption-desorption isotherms (Figures S4 and 2g). The specific surface areas of HC@PC–P, HC, and PC are 5.5 m^2 g^{-1}, 0.9 m^2 g^{-1} and 24.9 m^2 g^{-1}, respectively, which is consistent with the observations from SEM images. The PC features a loose and porous structure with an average pore size of 46.5 nm, HC has a smoother and denser
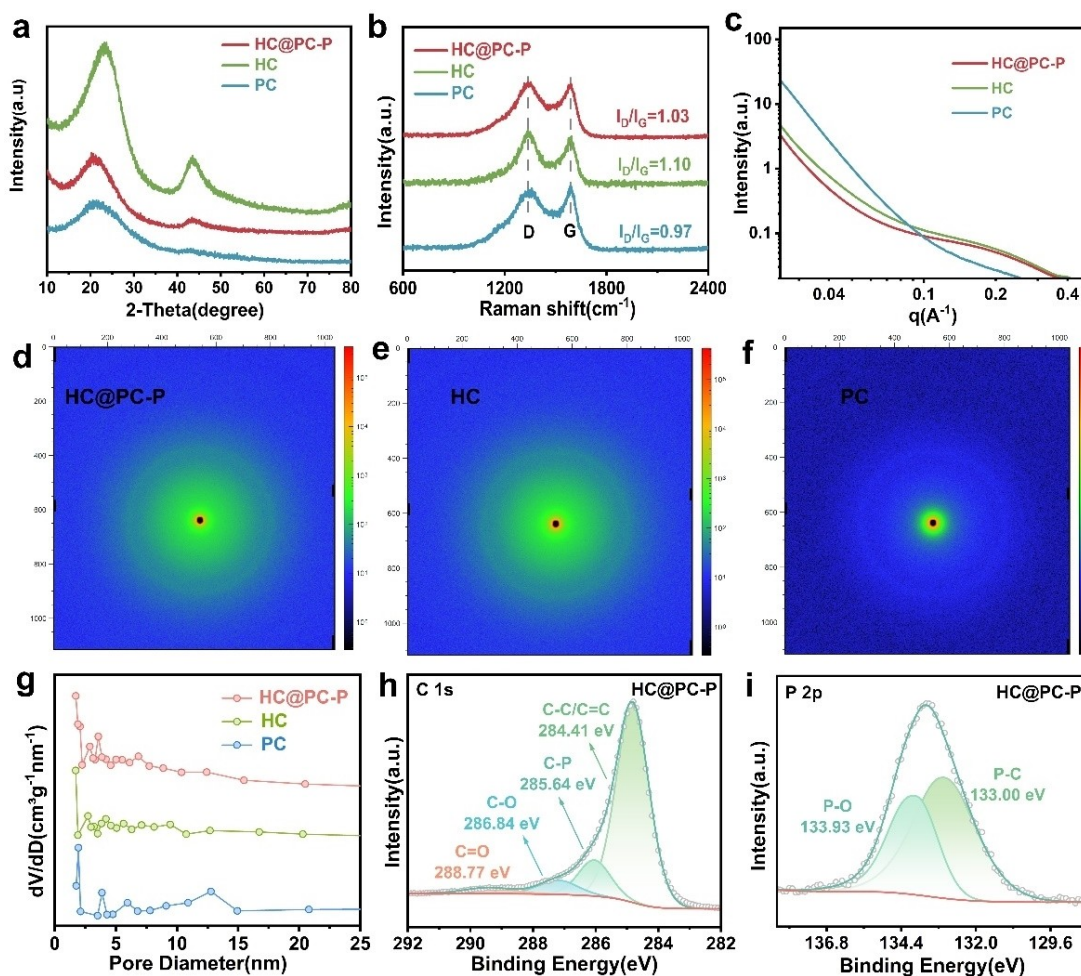
Figure 2. Structral characterization of prepared samples. a) XRD patterns, b) Raman spectrum, c) SAXS patterns, d–f) Wide-angle diffraction patterns and g) Pore size distributions of HC@PC–P, HC and PC. h) High-resolution C 1s and i) P 2p XPS spectra of HC@PC–P.

surface with an average pore size of 8.5 nm, while HC@PC–P exhibits an average pore size of 15.2 nm, falling between the two. The PC layer on the surface of HC not only facilitates electrolyte infiltration but also creates open Na$^+$ transport channels, significantly enhancing the diffusion rate of Na$^+$.[43] Moreover, this structure helps mitigate the volume changes of hard carbon during charge and discharge cycles, which is crucial for improving the cycle life of the battery.

XPS was employed to determine the elemental composition and oxidation states on the material surface (Figures 2 and S5–7). The high-resolution C 1s spectrum of HC@PC–P consists of four peaks: C–C/C=C (284.41 eV), C–P (285.64 eV), C–O (286.84 eV), and C=O (288.77 eV) (Figure 2h).[44] The O 1s spectrum is divided into three peaks: C=O (531.11 eV), C–O (532.36 eV), and O–C=O (533.63 eV).[45] Notably, the introduction of PC increases the content of C=O bonds in HC@PC–P compared to HC. The P 2p spectrum is deconvoluted into two peaks: P–C (133 eV) and P–O (133.93 eV), confirming the successful coating of the phosphorus-containing porous carbon layer (Figure 2i).[46–47]

The electrochemical performances of HC, PC, and HC@PC–P were compared by pairing the samples with sodium anodes.

The CV curves of HC and HC@PC–P at a scan rate of 0.1 mV·s^{-1} within the voltage range of 0.01–2.5 V are shown in Figures S8a and S8b. The initial CV curve of HC shows an irreversible broad band in the range of 0.16–1.0 V, which is related to the irreversible consumption of Na$^+$ and the formation of the solid electrolyte interface (SEI) film in the first cycle.[48] However, this broad band completely disappears in the CV curve of HC@PC–P, indicating the elimination of side reactions. At a low potential (0–0.1 V), a pair of sharp redox peaks appear due to the insertion/extraction of sodium ions between the graphite layers.[49] The CV curve of PC at 0.1 mV s^{-1} is shown in Figure S8c, where an irreversible peak also appears in the range of 0.16 to 1.0 V, but no obvious redox peaks are observed in the low potential range. This indicates that sodium ion intercalation does not occur in PC, consistent with the absence of a plateau region in the charge-discharge curve shown in Figure 3c.[50] In the subsequent two cycles, the CV curves of HC and HC@PC–P are highly coincident, indicating good reversibility during the cycling process. The first three galvanostatic charge-discharge (GCD) curves of HC, and HC@PC–P at a current density of 0.1 A g^{-1} are shown in Figures 3a and 3b, revealing two typical voltage regions: the high-voltage slope region (0.1 to 2.5 V,
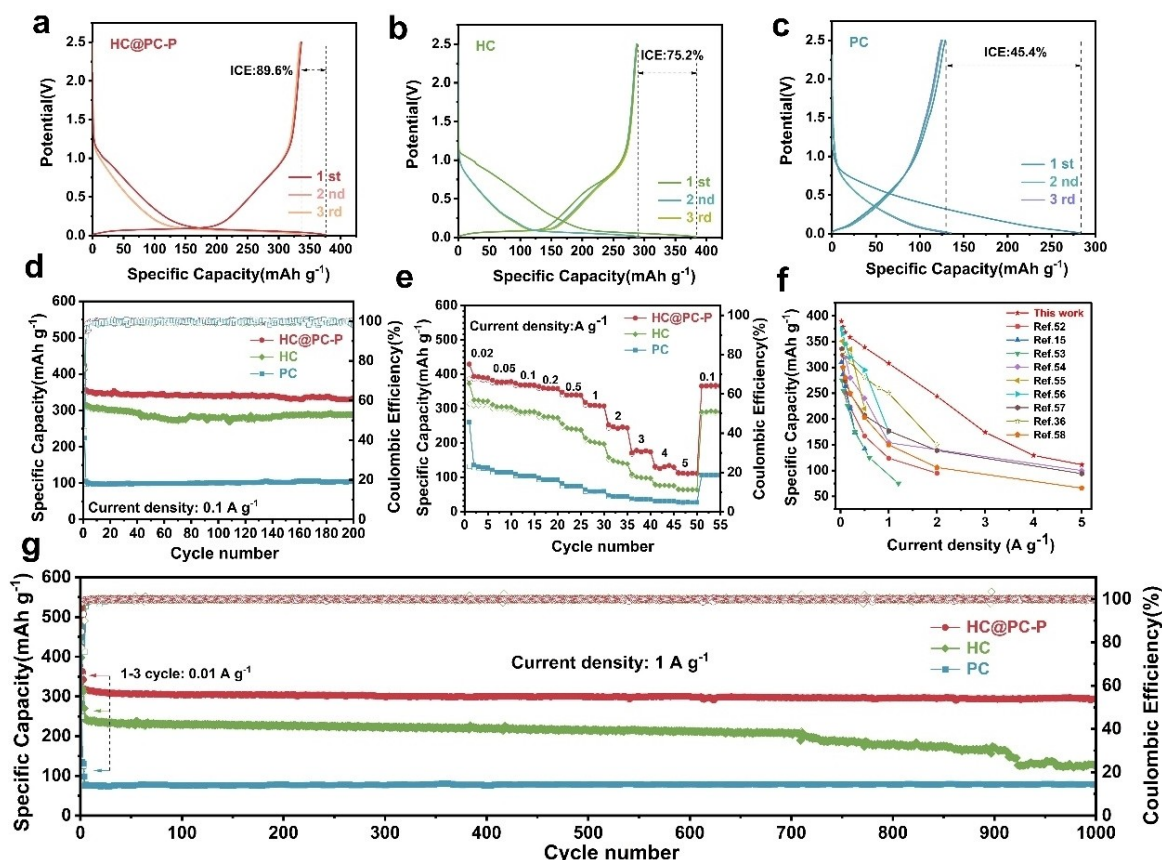
Figure 3. The first three GCD curves at a current rate of 0.1 A g^{-1} for a) HC@PC–P, b) HC, c) PC. d) Cyclic performance at 0.1 A g^{-1} and e) rate capability for HC@PC–P, HC and PC. f) Comparisons of rate performances. g) Long-life cyclic performance at 1 A g^{-1} for HC@PC–P, HC and PC.

corresponding to the adsorption of Na$^+$ on the surface, edges, and defect structures) and the low-voltage plateau region (0.01 to 0.1 V, corresponding to the filling of Na$^+$ between carbon layers and in closed pore structures).[20,51] Consistent with the CV results, PC shows a large irreversible capacity in the first cycle, with a very low ICE of only 45.4%, resulting in a low initial charge capacity (ICC) of 128 mAh g^{-1}. The initial three cycle GCD curves of the HC@PC–P anode are almost overlapping, and the degree of overlap is higher compared to the HC anode, indicating better Na$^+$ storage reversibility. In addition, HC@PC–P shows impressive initial discharge and charging specific capacities of 375.5 and 336.6 mAh g^{-1}, respectively. Therefore, the HC@PC–P shows a higher ICE of 89.6% compared to the HC anode (75.2%). This improvement is mainly attributed to the P doped porous carbon layer, which significantly reduces surface defects on HC, leading to the formation of fewer and more stable SEI films during the initial GCD process.

Figure 3d shows the stability test results after 200 cycles at a current of 0.1 A g^{-1}. Notably, the final specific capacity of the HC@PC–P anode after 100 cycles is as high as 340 mAh g^{-1}, significantly exceeding that of the HC anode (290 mAh g^{-1}) and the PC anode (100 mAh g^{-1}). The superior performance of HC@PC–P is due to P doping, which expands the interlayer spacing, allowing for greater accom-

modation of sodium ions in the low-voltage plateau region. Moreover, the morphology of HC@PC–P still maintains its original structure after a long cycle of charge and discharge (Figure S9), indicating that it has excellent structural stability. The rate performance of HC, PC, and HC@PC–P was further evaluated, as shown in Figure 3e. The capacities of HC@PC–P at 0.02, 0.05, 0.1, 0.2, 0.5, 1.0, 2.0, 3.0, 4.0, and 5.0 A g^{-1} are 389.2, 378.5, 368.4, 358.7, 338.8, 307.7, 244.0, 174.2, 129.5, and 111.4 mAh g^{-1}, respectively, while the cycle capacities of HC and PC at the same current densities are 311.9, 304.4, 291.4, 273.6, 238.6, 214.5, 158.5, 97.3, 75.7, and 64.4 mAh g^{-1} and 129.1, 114.9, 104.7, 93.0, 75.0, 59.4, 44.4, 35.8, 30.9, and 27.0 mAh g^{-1}, respectively. Obviously, HC@PC–P exhibits better rate performance than both HC and PC at all tested current densities, attributed to enhanced reaction kinetics. Even at a high current density of 5.0 A g^{-1}, HC@PC–P retains a capacity of 111.4 mAh g^{-1}, while HC only reaches 64.4 mAh g^{-1}. Notably, when the current density is returned to 0.1 A g^{-1}, the capacity recovers to 366.8 mAh g^{-1}, indicating that HC@PC–P demonstrates outstanding rate performance compared to previously reported hard carbon materials, particularly at high current densities, while also maintaining good reversibility and excellent structural stability (Figure 3f).[15,36,52–58] Finally, to further verify the durability and stability of HC, PC, and

HC@PC–P, a long cycle performance test was carried out at a current of 1 A g^{-1} (as shown in Figure 3g). The results show that HC@PC–P retains a high capacity of 294.8 mAh g^{-1} after 1000 cycles, corresponding to a capacity retention rate of 93.9%. In contrast, HC cycles stably at a lower specific capacity of 208.7 mAh g^{-1} for about 700 cycles before experiencing significant capacity attenuation. After 1000 cycles, its capacity declines to only 128.6 mAh g^{-1}, equating to a retention rate of 60.1%. Although PC shows a capacity retention rate close to 100%, its capacity remains low at 78.8 mAh g^{-1}. Moreover, the cycling performance presents a significant advantage compared to those reported in the literature (Table S2). These results indicate that the sodium storage performance of hard carbon materials is influenced by various factors, including microstructure (such as pore structure and interlayer spacing), electron transfer behavior, heteroatom presence, and defect content. Compared with HC, higher specific surface area of PC leads to the irreversible consumption of more sodium ions during SEI formation, resulting in relatively low capacity. HC@PC–P demonstrates excellent rate perform-

ance and cycle stability, primarily due to the presence of mesopores and macropores that facilitate electrolyte-carbon contact. These pores provide channels for sodium ion diffusion, while the introduction of P atoms not only expands the interlayer spacing but also enhances conductivity, enabling faster reaction kinetics.

To investigate the sodium storage mechanism of HC@PC–P, ex-situ Raman analysis was performed. As shown in Figure 4a–4c, the position of the D band remained almost unchanged during the discharge process, but its intensity gradually weakened, the peak broadened. The I$_D$/I$_G$ ratio decreased from 0.95 to 0.88, indicating a gradual reduction in defect sites, corresponding to Na$^+$ adsorption at these defects.[59] During discharge down to 0.5 V, the position of the G band remained relatively stable, while a significant redshift in the G band was observed at 0.1 V, indicating that charge transfer occurred within the carbon structure and corresponding to the intercalation of Na$^+$ between layers.[60] After 0.1 V, the G band position stabilized, reflecting the pore-filling process.[61] In summary, the sodium storage mechanism of HC@PC–P consists mainly of adsorption (2.5–
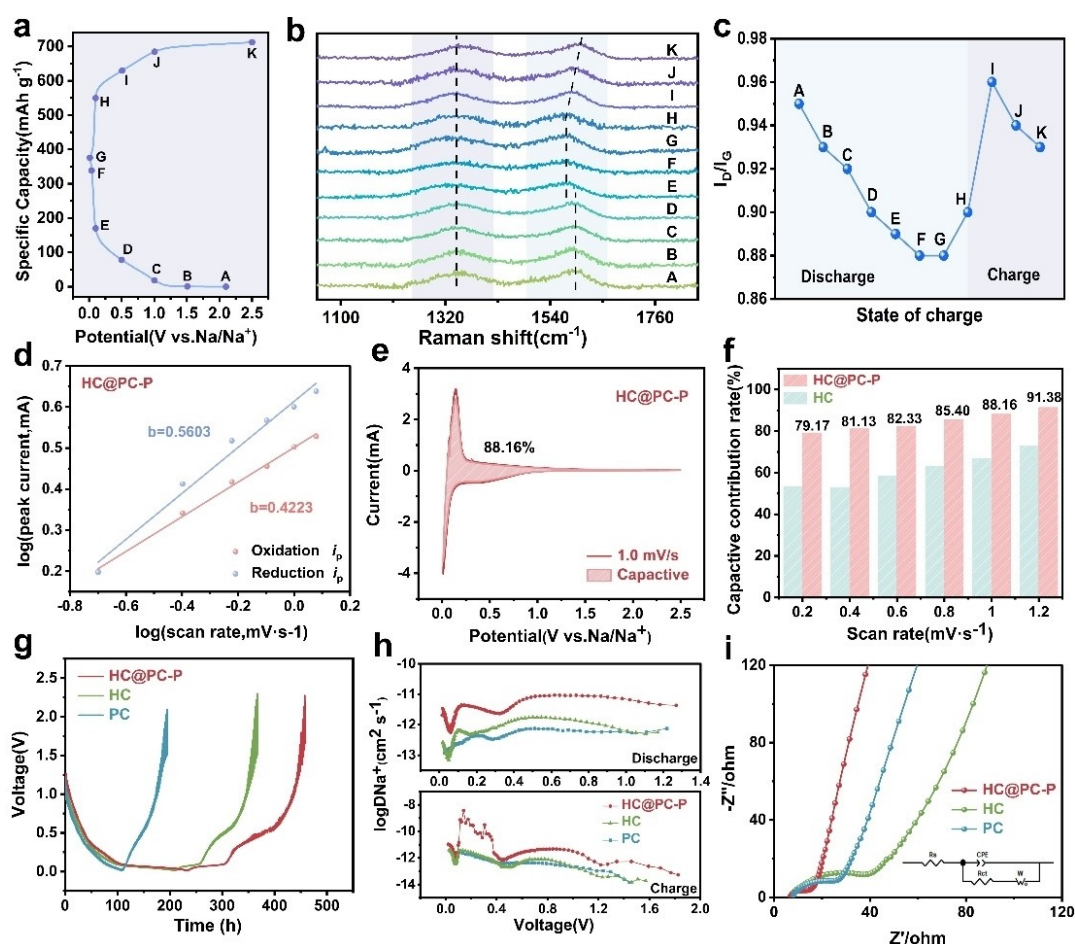
Figure 4. a) Galvanostatic charge-discharge curve and b) ex-situ Raman spectra of HC@PC–P in the initial cycle at the current density of 50 mA g^{-1}, c) The integrated density ratio of I$_D$/I$_G$ at different states of sodiation/desodiation. d) Plots of log(scan rate) versus log(peak current),calculated from CV curves. e) The detailed pseudocapacitive contribution of HC@PC–P at 1 mV s^{-1}. f) The percentages of pseudocapacitive contribution of HC@PC–P and HC electrode at different scan rates. g)GITT curves of HC@PC–P, HC and PC anodes and h) Na$^+$ diffusion coefficients during the sodiation and desodiation process. i) The electrochemical impedance spectra for HC@PC–P, HC and PC.

Batteries & Supercaps

Research Article
doi.org/10.1002/batt.202400694

Chemistry Europe
European Chemical
Societies Publishing

0.5 V), intercalation/adsorption (0.5–0.1 V), and pore filling (0.1–0.01 V). Additionally, the D and G bands reverted to their initial positions after charging, and the I_D/I_G ratio recovered to 0.93, confirming the excellent structural stability of HC@PC–P during the highly reversible sodiation/desodiation process.

In order to deeply study the sodium storage mechanism and kinetic behavior of all sample electrodes, different cyclic voltammetry (CV) curves with scanning rates in the range of 0.2-1.2 mVs^{-1} were tested (Figure S10, S11a, and S11b). The peak position of HC@PC–P changes little with the increase of scanning rate, indicating minimal polarization across different speeds. scanning speeds. As shown in Figure 4d, S11c, and S11d, there is a linear relationship between the logarithm of peak current (ip) and scanning rate (v). After calculation, the b values of samples HC, PC, and HC@PC–P at the oxidation peak are 0.36, 0.61, and 0.42 respectively, and at the reduction peak are 0.42, 0.82, and 0.56 respectively. The b value of the HC@PC–P electrode is higher than that of HC, indicating that through the modification with PC, the reaction can shift from being purely diffusion-controlled to a simultaneous control by both pseudocapacitance and diffusion. The capacitive contributions of HC@PC–P can be quantitatively distinguish, which gradually increases with the rising, as shown in Figure 4f. The capacitive contribution ratio reaches 88% at a sweep rate of 1.0 mVs^{-1} (Figure 4e). In contrast, the capacitance contribution of HC is relatively small (Figure S12), indicating that its main contribution is intercalation. From the structural perspective, the porous carbon layer reduces the sodium ion diffusion path and increases the reaction rate. Meanwhile, the introduction of P atoms also enhances the electrical conductivity and promotes electron transfer. Consequently, HC@PC–P exhibits a capacitance-controlled sodium storage behavior.

In addition, in order to further study the diffusion reaction of sodium ions in HC, PC, and HC@PC–P, the galvanostatic intermittent titration technique (GITT) was used (Figure 4g). During the discharge process, the diffusion coefficient of sodium ions in HC@PC–P continuously decreases as the potential approaches 0 V, which is also observed in HC. Conversely, during the charging process, the diffusion coefficient exhibits an opposite trend (Figure 4h), further demonstrating the reversibility of sodium ion diffusion. Throughout the entire process, the diffusion coefficient of sodium ions in HC@PC–P (4.34×10^{-12}) is greater than that in HC (5.64×10^{-13}), indicating that P doping enhances the electronic structure of hard carbon, increases active sites, and facilitates the rapid diffusion of sodium ions. Figure 4i shows the Nyquist plot of HC@PC–P, along with two control samples HC and PC. All Nyquist plots display a semicircle in the medium-high frequency region, representing the charge transfer resistance (R_{ct}), and a straight line in the low frequency region, which corresponds to the Warburg diffusion resistance (W).[62] The data obtained from fitting the equivalent circuit reveals that the R_{ct} of HC@PC–P is 12.1 Ω, lower than 31.0 Ω of PC and

48.8 Ω of HC. This indicates that P doping reduces charge transfer resistance and accelerates electron transfer. In addition, the Warburg resistance stems from the diffusion of Na$^+$ in the electrode material. As can be seen from Figure S13, the Warburg factor values of HC, PC, and HC@PC–P are 503.8, 456.3, and 270.1 respectively. The corresponding D_{Na+} are calculated to be 9.84×10^{-15}, 1.20×10^{-14} cm^{2}s^{-1}, and 3.42×10^{-14} cm^{2}s^{-1} respectively. Obviously, HC@PC–P exhibits a higher diffusion coefficient and a lower R_{ct} value, indicating faster electrochemical kinetics.

The results above clearly show that the sodium storage mechanism of HC@PC–P involves three main stages: adsorption (2.5–0.5 V), intercalation/adsorption (0.5–0.1 V), and pore filling (0.1 V–0.01 V). Initially, during the adsorption stage, sodium ions are adsorbed onto the surface and defect sites of the material, which enables rapid ion storage and enhances fast-charging capabilities. The porous carbon layer also serves as a conduit for ion transport and contributes to sodium ion storage through adsorption within the pores. Secondly, the distinct pseudo-graphite stripes and expanded interlayer spacing in HC@PC–P facilitate sodium ion insertion and enhance capacity in the sloping region during the intercalation/adsorption stage. Furthermore, phosphorus doping increases the proportion of pseudo-capacitance for HC@PC–P, which further accelerates sodium ion adsorption and improves rate performance. Lastly, the abundance of closed pores in HC@PC–P provides fast diffusion channels and storage sites for sodium ions during the pore filling stage, significantly increasing the plateau capacity.

In order to explore the practical application of HC@PC–P in SIBs, $Na_3V_2(PO_4)_3$ (NVP) as the cathode material to match with HC@PC–P for the assembly of button-type full batteries (Figure 5a). In Figure 5b charge-discharge curves of the high-voltage NVP cathode and HC@PC–P anode is tested to evaluate the practical feasibility. As shown in Figure 5c, the charge-discharge curves of the HC@PC–P//NVP full battery during the first three cycles display a sloping shape within the voltage range of 1.5 to 3.8 V at 0.1 Ag^{-1}, with a stable discharge capacity reaching 80.6 mAhg^{-1}. As shown in Figure 5d, the discharge capacity of the HC@PC–P//NVP full battery remains at 79.1 mAhg^{-1} after 100 cycles, resulting in a capacity retention rate of 94.2% compared to the first cycle, which underscores the stability of the battery. Figure 5e and S14 further highlights the excellent rate performance of HC@PC–P//NVP. As the current density increases from 0.05 Ag^{-1} to 0.1, 0.2, 0.5, 1, 2, and 5 Ag^{-1}, the reversible capacity gradually decreases to 97.4, 95.9, 89.9, 80.8, 75.9, 67.1 and 50.2 mAhg^{-1}, respectively. When the current density returns to 0.1 Ag^{-1}, the capacity recovers to 84.6 mAhg^{-1}. The long-term cycling performance of HC@PC–P//NVP at 1 Ag^{-1} is depicted in Figure 5g. Even after 300 cycles, a reversible capacity of 54.3 mAhg^{-1} can still be obtained. At this high current density, the Coulombic efficiency is close to 100%, with a capacity retention rate is 78.26%. The calculated energy and power densities of the HC@PC–P//NVP full cell are illustrated in Figure 5f. Notably,
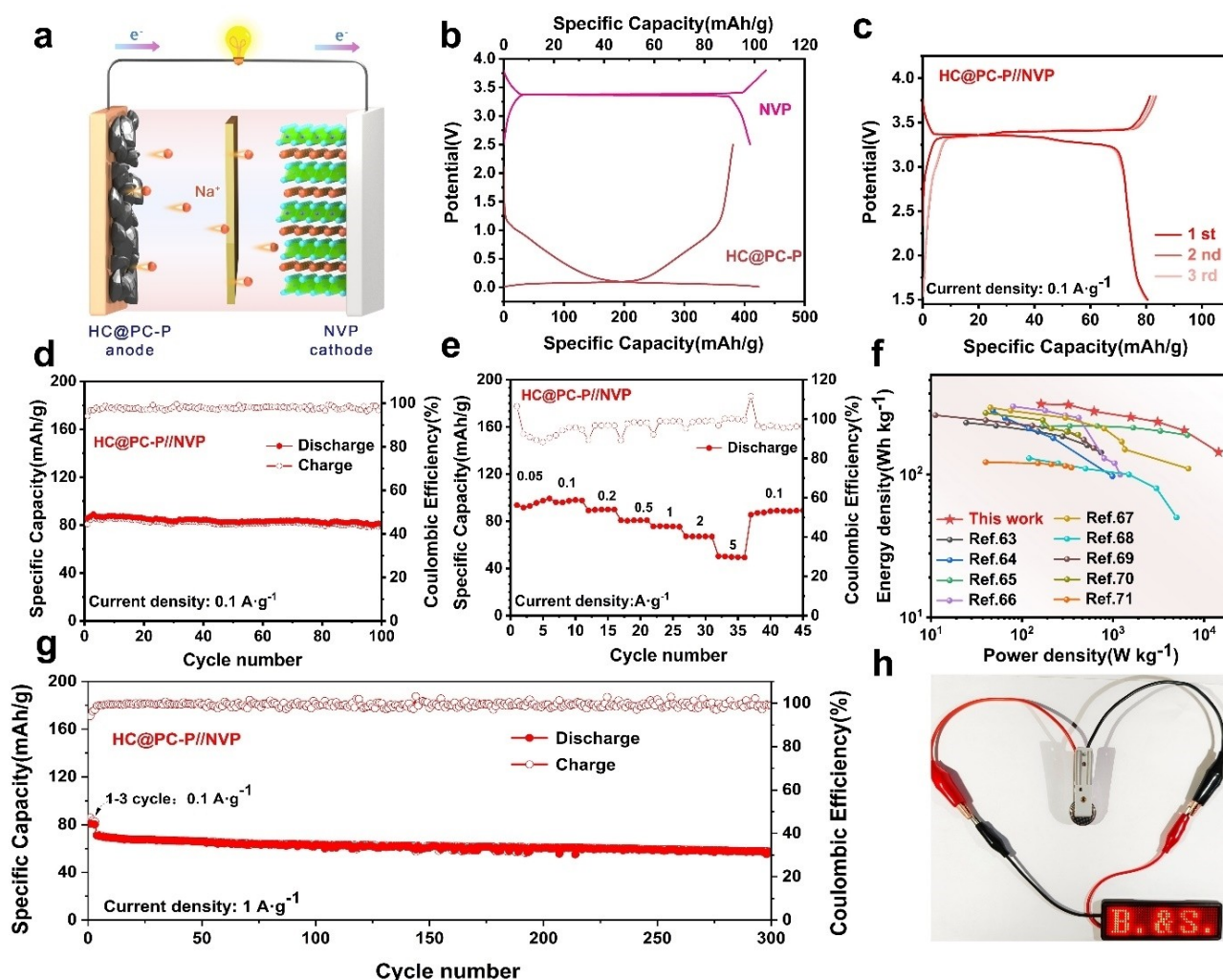
Figure 5. a) Schematic illustration of the as-assembled HC@PC–P//NVP full-cell. b) The initial GCD curves of NVP//Na half-cell and HC@PC–P//Na half-cell at 0.1 A g^{-1}, respectively. c) The GCD curves of HC@PC–P//NVP full-cell in the first 3 cycles. d) The cycling performance of HC@PC–P//NVP full-cell at 0.1 A g^{-1}. e) The rate performance of HC@PC–P//NVP full-cell. f) Energy density and power density of the full cell compared with previously reported SIBs full cell at various current densities. g) A digital photograph of LEDs powered by the cell battery.

the energy density of the assembled battery reaches 257.9 Wh kg^{-1} at 320 W kg^{-1} (based on the mass of the cathode and anode) and remains at 143.5 Wh kg^{-1} at 14.5 KW kg^{-1}, surpassing many leading sodium-ion full batteries reported in the literature.[51,63–70] As shown in Figure 5h, the HC@PC–P//NVP full battery is capable of lighting up LED bulbs simultaneously, further demonstrating its potential value in practical applications.

Conclusions

In summary, a surface-porous phosphorus-doped hard carbon material (HC@PC–P) has been successfully synthesized using a surface thermal polymerization method, employing discarded olive kernels and soybean lecithin as precursors. The enhancements in electrical conductivity, interlayer spacing, and porous structure contribute to impressive rate performance and long cycle stability of

HC@PC–P. Notably, it can maintain a high capacity of 294.8 mAh g^{-1} can be maintained at 1 A g^{-1} after 1000 cycles. Additionally, structural adjustments have resulted in a relatively high ICE of 89.6%. A series of analyses demonstrate that the unique pore structure, combined with P doping, promotes the diffusion of sodium ions. Importantly, the assembled HC@PC–P//NVP full battery achieves an energy density as high as 257.9 Wh kg^{-1}. These fundamental findings provide a straightforward method for producing hard carbon materials with excellent storage performance, positioning a widespread use in the field of energy storage.

Acknowledgements

Conflict of Interests

The authors declare no conflict of interest.

Data Availability Statement

The data that support the findings of this study are available from the corresponding author upon reasonable request.

[1] A. Q. Al-Shetwi, *Sci. Total Environ.* **2022**, *822*, 153645.
[2] Y. Chen, Y. Kang, Y. Zhao, L. Wang, J. Liu, Y. Li, Z. Liang, X. He, X. Li, N. Tavajohi, B. Li, *J. Energy Chem.* **2021**, *59*, 83–99.
[3] R. Shao, Z. Sun, L. Wang, J. Pan, L. Yi, Y. Zhang, J. Han, Z. Yao, J. Li, Z. Wen, S. Chen, S. Chou, D.-L. Peng, Q. Zhang, *Angew. Chem. Int. Ed.* **2024**, *63*, e202320183.
[4] W. Zhang, J. Lu, Z. Guo, *Mater. Today* **2021**, *50*, 400–417.
[5] J. Wang, J. Li, Q. Zhang, W. Du, H. M. Abo-Dief, S. Melhi, R. Sellami, J. Guo, C. Hou, X. Sun, *Adv. Compos. Hybrid Mater.* **2024**, *7*, 119.
[6] S. Qiao, Q. Zhou, M. Ma, H. K. Liu, S. X. Dou, S. Chong, *ACS Nano* **2023**, *17*, 11220–11252.
[7] Y. Wan, B. Huang, W. Liu, D. Chao, Y. Wang, W. Li, *Adv. Mater.* **2024**, *36*, e2404574.
[8] C. Nita, B. Zhang, J. Dentzer, C. Matei Ghimbeu, *J. Energy Chem.* **2021**, *58*, 207–218.
[9] L. Wu, D. Buchholz, C. Vaalma, G. A. Giffin, S. Passerini, *ChemElectroChem* **2016**, *3*, 292–298.
[10] J. Xiang, W. Lv, C. Mu, J. Zhao, B. Wang, *J. Alloys Compd.* **2017**, *701*, 870–874.
[11] N. Sun, H. Liu, B. Xu, *J. Mater. Chem. A* **2015**, *3*, 20560–20566.
[12] Z. Zheng, S. Hu, W. Yin, J. Peng, R. Wang, J. Jin, B. He, Y. Gong, H. Wang, H. J. Fan, *Adv. Energy Mater.* **2023**, *14*, 2303064.
[13] K. Kim, D. G. Lim, C. W. Han, S. Osswald, V. Ortalan, J. P. Youngblood, V. G. Pol, *ACS Sustainable Chem. Eng.* **2017**, *5*, 8720–8728.
[14] Q. Jiang, Z. Zhang, S. Yin, Z. Guo, S. Wang, C. Feng, *Appl. Surf. Sci.* **2016**, *379*, 73–82.
[15] X. Zhao, Y. Ding, Q. Xu, X. Yu, Y. Liu, H. Shen, *Adv. Energy Mater.* **2019**, *9*, 1803648.
[16] Y. Feng, L. Tao, Y. He, Q. Jin, C. Kuai, Y. Zheng, M. Li, Q. Hou, Z. Zheng, F. Lin, H. Huang, *J. Mater. Chem. A* **2019**, *7*, 26954–26965.
[17] D. Alvira, D. Antorán, J. J. Manyà, *Chem. Eng. J.* **2022**, *447*, 137468.
[18] M. Thompson, Q. Xia, Z. Hu, X. S. Zhao, *Mater Adv* **2021**, *2*, 5881–5905.
[19] L. Xie, C. Tang, Z. Bi, M. Song, Y. Fan, C. Yan, X. Li, F. Su, Q. Zhang, C. Chen, *Adv. Energy Mater.* **2021**, *11*, 2101650.
[20] N. Sun, J. Qiu, B. Xu, *Adv. Energy Mater.* **2022**, *12*, 2200715.
[21] H. Wang, C.-J. Yao, H.-J. Nie, K.-Z. Wang, Y.-W. Zhong, P. Chen, S. Mei, Q. Zhang, *J. Mater. Chem. A* **2020**, *8*, 11906–11922.
[22] M. Zhang, Y. Li, F. Wu, Y. Bai, C. Wu, *Nano Energy* **2021**, *82*, 105738.
[23] T. Perveen, M. Siddiq, N. Shahzad, R. Ihsan, A. Ahmad, M. I. Shahzad, *Renewable Sustainable Energy Rev.* **2020**, *119*, 109549.
[24] Y. Yang, C. Wu, X. X. He, J. Zhao, Z. Yang, L. Li, X. Wu, L. Li, S. L. Chou, *Adv. Funct. Mater.* **2023**, *34*, 2302277.
[25] K. Z. Cao, Y. N. He, S. T. Wang, J. J. Fu, H. Liu, *Journal of Xinyang Normal University Natural Science Edition* **2024**, *37*, 154–159.
[26] D. Chen, W. Zhang, K. Luo, Y. Song, Y. Zhong, Y. Liu, G. Wang, B. Zhong, Z. Wu, X. Guo, *Energy Environ. Sci.* **2021**, *14*, 2244–2262.
[27] J. Liu, Y. You, L. Huang, Q. Zheng, Z. Sun, K. Fang, L. Sha, M. Liu, X. Zhan, J. Zhao, Y. C. Han, Q. Zhang, Y. Chen, S. Wu, L. Zhang, *Adv. Mater.* **2024**, *36*, 2407369.
[28] T. Tang, W. Zhu, P. Lan, X. Lan, H. Xie, P. K. Shen, Z. Q. Tian, *Chem. Eng. J.* **2023**, *475*, 146212.
[29] H. Lu, X. Chen, Y. Jia, H. Chen, Y. Wang, X. Ai, H. Yang, Y. Cao, *Nano Energy* **2019**, *64*, 103903.
[30] K. Luo, D. Wang, D. Chen, Y. Zhong, Z. Zheng, G. Wang, Y. Liu, B. Zhong, Z. Wu, X. Guo, *ACS Appl. Energ. Mater.* **2021**, *4*, 8242–8251.
[31] Y. Yuan, Z. Chen, H. Yu, X. Zhang, T. Liu, M. Xia, R. Zheng, M. Shui, J. Shu, *Energy Storage Mater.* **2020**, *32*, 65–90.
[32] X. Feng, Y. Bai, M. Liu, Y. Li, H. Yang, X. Wang, C. Wu, *Energy Environ. Sci.* **2021**, *14*, 2036–2089.
[33] W. Ge, *Journal of Xinyang Normal University Natural Science Edition* **2024**, *37*, 147–153.
[34] Q. Jin, K. Wang, P. Feng, Z. Zhang, S. Cheng, K. Jiang, *Energy Storage Mater.* **2020**, *27*, 43–50.
[35] S. Zhong, H. Liu, D. Wei, J. Hu, H. Zhang, H. Hou, M. Peng, G. Zhang, H. Duan, *Chem. Eng. J.* **2020**, *395*, 125054.
[36] Z. Zhang, G. Li, G. Liang, P. Zhao, X. Gong, J. Dai, H. Xiong, Z. Zhang, J. Mao, S. Zhang, B. Wang, *Batteries & Supercaps* **2024**, *7*, e202300552.
[37] H. Zhang, W. Zhang, F. Huang, *Chem. Eng. J.* **2022**, *434*, 134503.
[38] H. Au, H. Alptekin, A. C. S. Jensen, E. Olsson, C. A. O'Keefe, T. Smith, M. Crespo-Ribadeneyra, T. F. Headen, C. P. Grey, Q. Cai, A. J. Drew, M.-M. Titirici, *Energy Environ. Sci.* **2020**, *13*, 3469–3479.
[39] Y. Morikawa, S. i. Nishimura, R. i. Hashimoto, M. Ohnuma, A. Yamada, *Adv. Energy Mater.* **2019**, *10*, 1903176.
[40] J. Yang, X. Wang, W. Dai, X. Lian, X. Cui, W. Zhang, K. Zhang, M. Lin, R. Zou, K. P. Loh, Q.-H. Yang, W. Chen, *Nano-Micro Lett.* **2021**, *13*, 98.
[41] Z. Tang, R. Zhang, H. Wang, S. Zhou, Z. Pan, Y. Huang, D. Sun, Y. Tang, X. Ji, K. Amine, M. Shao, *Nat. Commun.* **2023**, *14*, 6024.
[42] Q. Meng, Y. Lu, F. Ding, Q. Zhang, L. Chen, Y.-S. Hu, *ACS Energy Lett.* **2019**, *4*, 2608–2612.
[43] H. Ye, S. Xin, Y. X. Yin, Y. G. Guo, *Adv. Energy Mater.* **2017**, *7*, 1700530.
[44] Z. Li, C. Bommier, Z. S. Chong, Z. Jian, T. W. Surta, X. Wang, Z. Xing, J. C. Neuefeind, W. F. Stickle, M. Dolgos, P. A. Greaney, X. Ji, *Adv. Energy Mater.* **2017**, *7*, 1602894.
[45] C. Chen, Y. Huang, M. Lu, J. Zhang, T. Li, *Carbon* **2021**, *183*, 415–427.
[46] S. Tao, W. Xu, J. Zheng, F. Kong, P. Cui, D. Wu, B. Qian, S. Chen, L. Song, *Carbon* **2021**, *178*, 233–242.
[47] S. Wu, X. Lu, K. Zhang, J. Xu, Z. Sun, *Batteries & Supercaps* **2022**, *6*, e202200427.
[48] Y. Li, B. Ni, X. Li, X. Wang, D. Zhang, Q. Zhao, J. Li, T. Lu, W. Mai, L. Pan, *Nano-Micro Lett.* **2019**, *11*, 60.
[49] W. Shao, F. Hu, C. Song, J. Wang, C. Liu, Z. Weng, X. Jian, *J. Mater. Chem. A* **2019**, *7*, 6363–6373.
[50] X. Yin, Y. Zhao, X. Wang, X. Feng, Z. Lu, Y. Li, H. Long, J. Wang, J. Ning, J. Zhang, *Small* **2022**, *18*, e2105568.
[51] X. Yin, Z. Lu, J. Wang, X. Feng, S. Roy, X. Liu, Y. Yang, Y. Zhao, J. Zhang, *Adv. Mater.* **2022**, *34*, 2109282.
[52] M.-X. Song, L.-J. Xie, J.-Y. Cheng, Z.-L. Yi, G. Song, X.-Y. Jia, J.-P. Chen, Q.-G. Guo, C.-M. Chen, *J. Energy Chem.* **2022**, *66*, 448–458.
[53] F. Xie, Z. Xu, A. C. S. Jensen, H. Au, Y. Lu, V. Araullo-Peters, A. J. Drew, Y. S. Hu, M. M. Titirici, *Adv. Funct. Mater.* **2019**, *29*, 1901072.
[54] H. Wang, W. Yu, J. Shi, N. Mao, S. Chen, W. Liu, *Electrochim. Acta* **2016**, *188*, 103–110.
[55] N. Zhang, Q. Liu, W. Chen, M. Wan, X. Li, L. Wang, L. Xue, W. Zhang, *J. Power Sources* **2018**, *378*, 331–337.
[56] Q. Wang, X. Zhu, Y. Liu, Y. Fang, X. Zhou, J. Bao, *Carbon* **2018**, *127*, 658–666.
[57] H. Liu, M. Jia, B. Cao, R. Chen, X. Lv, R. Tang, F. Wu, B. Xu, *J. Power Sources* **2016**, *319*, 195–201.
[58] H. W. Jia Ding, Z. Li, A. Kohandehghan, K. Cui, Z. Xu, B. Zahiri, X. Tan, E. Memarzadeh Lotfabad, B. C. Olsen, D. Mitlin, *ACS Nano* **2013**, *7*, 11004–11015.
[59] X. X. He, W. H. Lai, Y. Liang, J. H. Zhao, Z. Yang, J. Peng, X. H. Liu, Y. X. Wang, Y. Qiao, L. Li, X. Wu, S. L. Chou, *Adv. Mater.* **2023**, *35*, e2302613.
[60] M. Anji Reddy, M. Helen, A. Groß, M. Fichtner, H. Euchner, *ACS Energy Lett.* **2018**, *3*, 2851–2857.
[61] N. S. Shaohong Zhang, X. Li, R. A. Soomro, B. Xu, *Energy Storage Mater.* **2024**, *66*, 103183.
[62] B. Padha, S. Verma, P. Mahajan, S. Arya, *J. Electrochem. Sci. Technol.* **2022**, *13*, 167–176.

[63] D. Sun, L. Zhao, P. Sun, K. Zhao, Y. Sun, Q. Zhang, Z. Li, Z. Ma, F. Zheng, Y. Yang, C. Lu, C. Peng, C. Xu, Z. Xiao, X. Ma, *Adv. Funct. Mater.* **2024**, *34*, 2403642.

[64] M. D. Zhenqi Song, S. Chen, Y. Bai, *Chem. Eng. J.* **2023**, *470*, 144237.

[65] Q. He, H. Chen, X. Chen, J. Zheng, L. Que, F. Yu, J. Zhao, Y. Xie, M. Huang, C. Lu, J. Meng, X. Zhang, *Adv. Funct. Mater.* **2024**, *34*, 2310226.

[66] B. Yin, S. Liang, D. Yu, B. Cheng, I. L. Egun, J. Lin, X. Xie, H. Shao, H. He, A. Pan, *Adv. Mater.* **2021**, *33*, 2100808.

[67] L. Liang, Y. Xu, C. Wang, L. Wen, Y. Fang, Y. Mi, M. Zhou, H. Zhao, Y. Lei, *Energy Environ. Sci.* **2015**, *8*, 2954–2962.

[68] C. Qiu, A. Li, D. Qiu, Y. Wu, Z. Jiang, J. Zhang, J. Xiao, R. Yuan, Z. Jiang, X. Liu, X. Chen, H. Song, *ACS Nano* **2024**, *18*, 11941–11954.

[69] M. R. Panda, A. Raj, K. A. Ghosh, A. Kumar, D. Muthuraj, S. Sau, W. Yu, Y. Zhang, A. K. Sinha, M. Weyland, Q. Bao, S. Mitra, *Nano Energy* **2019**, *64*, 103951.

[70] Z. Lu, J. Wang, W. Feng, X. Yin, X. Feng, S. Zhao, C. Li, R. Wang, Q. A. Huang, Y. Zhao, *Adv. Mater.* **2023**, *35*, e2211461.